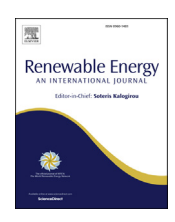


Contents lists available at ScienceDirect

Renewable Energy

journal homepage: www.elsevier.com/locate/renene



Tidal turbine performance and near-wake characteristics in a sheared turbulent inflow



Ashwin Vinod, Cong Han, Arindam Banerjee*

Department of Mechanical Engineering & Mechanics, Lehigh University, Bethlehem, PA, USA

ARTICLE INFO

Article history:
Received 29 November 2020
Received in revised form
4 April 2021
Accepted 4 May 2021
Available online 11 May 2021

Keywords: Sheared turbulent inflows Tidal stream turbine Near-wake Performance characteristics Active grid

ABSTRACT

Turbulent non-homogenous flow environments at high-energy tidal sites lead to variation in power performance of tidal stream turbines. In addition, non-uniform loading due to combined effects of shear and elevated inflow turbulence affects device survivability. In the current study, an active-grid turbulence generator is used to mimic sheared-turbulent inflow representative of the flood (low shear) and ebb tides (high shear). The performance and near-wake characteristics of a turbine model measured in the sheared-turbulent inflow conditions are compared to conditions where the flow velocity is uniform with low and elevated turbulence intensities (T_i). The sheared-turbulent inflows were observed to result in a 5–15% drop in maximum power coefficient when compared to the low T_i case. An increase of ~30% in torque- and ~50% in thrust- fluctuations were observed for sheared inflows. Unlike the near axisymmetric wake profiles observed for homogeneous cases, inflow shear was observed to incite asymmetry in the near-wake with an immediate impact in wake turbulence and a more gradual effect on the velocity deficit and integral length scales. The data sets are deemed valuable in calibrating computational models to better predict turbine response and optimize turbine efficiency and the complementing power take-off system.

© 2021 Elsevier Ltd. All rights reserved.

1. Introduction

Tides, driven by the gravitational interaction of the Earth-Moon-Sun system, is a very promising renewable energy resource offering high energy density and ~98% predictability for decades [1]. Building on the learnings from the more mature wind turbine technologies, tidal stream turbines (TST) has advanced rather quickly, with multiple commercial arrays under construction in Europe [1] and the United States [2,3]. Individual turbines installed in the proposed commercial projects have diameters between 5 and 25 m with a rated power output between 35kW and 2MW [1]. With the knowledge and experience gained in various fundamental aspects relating to the technology over the last decade, the focus of ongoing research in TSTs is shifting towards addressing questions related to the commercial-scale deployment of TST arrays. These questions include understanding the implications of free stream turbulence [4-8], free surface proximity [9-11], wake interactions [12–14], and inflow misalignment [15–18]. In addition to being three-dimensional and turbulent, flow conditions occurring in the tidal estuaries and rivers are often non-uniform owing to wave current interactions [19] and secondary flows resulting from bathymetry features and instream structures [20,21]. The bottommounted configuration of most of the existing TST designs [1] makes them susceptible to benthic boundary layer effects as well [22]. Spatial variations in inflow characteristics within the energy capture area of a TST would alter the hydrodynamic forces and available power across rotor area, resulting in significant engineering implications to the structural loads, operational life, annual energy production, electrical grid integration, and cost of energy [20,23]. Therefore, the consequences of such flow conditions within a potential deployment site must be well understood to ensure operational efficiency and survivability of installed devices. Based on the knowledge of the authors, there are only a couple of studies that have explored the effects of sheared inflows on a TST's. Rourke et al. [24] used an unsteady BEM model to perform a hydrodynamic analysis of a tidal current turbine in tidal current shear. They simulated multiple sheared inflow profiles and observed significant asymmetric loading on the rotor blade sections. Ahmed et al. [25] performed geometry resolved simulations of a full-scale (18m diameter) 1 MW tidal turbine deployed in a sheared inflow at the

^{*} Corresponding author. Mechanical Engineering & Mechanics, 19 Memorial Drive West, Lehigh University, Bethlehem, PA, 18015, USA.

E-mail address: arb612@lehigh.edu (A. Banerjee).

European Marine Energy Cite (EMEC) to compare the efficacy of RANS (Reynolds Averaged Navier Stokes) and LES (Large Eddy Simulations) computational models in predicting the fluctuating loads acting on the turbine captured during the deployment. They concluded that the RANS approach was sufficient to capture mean loads acting on the rotor: however, LES with synthetic inflow turbulence was more effective in reproducing the full frequency range of bending moment fluctuations experienced by the rotor blades. They also briefly discussed the wake characteristics of the turbine obtained through the simulations but were unable to validate it with experimental results due to the unavailability of such data sets. Tedds et al. [8] performed a controlled laboratory-scale experimental study testing the effects of three different inflow conditions, uniform flow with 2% turbulence intensity, uniform flow with 5% turbulence intensity, and a non-uniform flow with 5% turbulence intensity on the performance and wake characteristics of a three-bladed tidal turbine model. They noted the minimal impact of the inflow profiles on turbine wake characteristics and time-averaged performance coefficients when nondimensionalized using the upstream integral average velocity.

Owing to the relevance of the problem to wind turbines, there is a rich body of literature that addresses questions related to the effects of atmospheric boundary layer [26] and stability [27] on the power capture capability of a wind turbine. We briefly review those relevant to our shear-flow study for tidal turbines. However, it is worthwhile to point out that the operating conditions of TST's are different compared to wind turbines, primarily because of the boundedness of the ambient flow due to the presence of a free surface. Wagner et al. [28] analyzed wind profiles that varied from high shear to no shear over flat terrain; the wind profiles were used as input to a Blade Element Momentum (BEM) model to analyze the sensitivity of the power generated by a turbine. The inflow wind profiles did not follow the logarithmic law and were found to strongly affect the kinetic energy flux; the electrical power generated by a turbine correlated significantly better to an equivalent wind speed than to a single point wind speed at hub height that is assumed for most studies. The effectiveness of the equivalent wind speed approach in reducing the power curve measurement uncertainty and improving annual energy production estimates was also verified using field experiments [29]. Kavari et al. [30] used a BEM-based approach to evaluate the effects of wind shear on the aerodynamic coefficients of airfoil sections along the length of the blade and found that effects of shear were most evident on sections between 20% and 80% of the blade span. Sezer-Uzol et al. [31] utilized a three-dimensional unsteady vortex panel method potential flow solver based on a free vortex wake methodology to quantify the influence of wind shear profiles on the performance and wake of a horizontal axis wind turbine. Wind-shear resulted in high levels of thrust-torque fluctuations on the turbine rotor and also resulted in an asymmetric wake with noticeable non-periodicities and non-uniformities.

The experimental work presented in this paper adds to the work by Tedds et al. [8] by investigating the implications of controlled, more extreme turbulent/sheared inflow conditions on the operational efficiency and near-wake flow features of a tidal turbine model. An active grid turbulence generator, conceptually similar to the one developed by Makita [32], is used to seed desired sheared-turbulent inflow conditions in the laboratory. The effects of sheared-turbulent inflows are explained in detail by comparing it to the trends observed in a previous work by the authors, which involved a homogeneous elevated turbulent inflow and a baseline quasi-laminar flow [4]. Turbine performance characteristics are discussed in terms of time-averaged power and thrust coefficients and their standard deviations. The influence of shear on the near-wake is characterized in terms of velocity deficit, wake swirl,

turbulence intensities, Reynolds stresses, integral length scales and periodicities. The capability to accurately predict turbine wakes is central to developing efficient TST array layouts. The near-wake experiments reported here provide data sets to validate, verify and refine numerical models of TST wake evolution in naturally occurring turbulent-sheared inflow conditions [33,47].

2. Experimental methods

All experiments presented herein were performed in the Tidal Turbulence Test facility (T^3F) housed at Lehigh University, Pennsylvania, USA. The water tunnel has an open surface test section with a length of 1.98m, a width of 0.61m, and a height of 0.61m. The maximum flow speed attainable within the test section at full depth is 1 m/s.

2.1. Turbulence generation and flow characterization

The water tunnel facility is equipped with a Makita-type active grid turbulence generator [32], as shown in Fig. 1a; the inner crosssection of the grid assembly precisely matched the dimensions of the water tunnel test section. The active grid module comprises five horizontally oriented shafts and five vertically oriented shafts. It is also capable of operating in an alternate 5 shaft configuration with five horizontal shafts only. Six square winglets $(0.06 \text{ m} \times 0.06 \text{ m})$ were attached to each shaft in such a fashion that one of their diagonals was parallel to the axis of the shaft. The adjacent shafts (in both horizontal and vertical directions) were separated by a distance of 0.1m (referred to as the mesh size, M). The horizontal and vertical shafts were set up in two separate planes (bi-planar configuration) 0.01m apart, and each shaft was controlled by a dedicated Anaheim Automation stepper motor (Model No. 23MDSI). In addition to rotating winglets, the active grid module also incorporates 24 stationary half winglets attached to the inner walls of the active grid upstream of the winglet shafts. Three forcing protocols, synchronous protocol (SP), single random protocol (SRP), and double random protocol (DRP) commonly used in literature, were programmed/implemented using a LabVIEW interface (the schematic of the protocols is shown in Fig. 1b [34]. In SP, the angular velocity is maintained uniform across all winglet shafts, and the adjacent shafts are programmed to rotate in opposite directions to forestall the occurrence of mean vorticity in the generated turbulent flow. SRP maintains a constant angular velocity across all shafts; however, it randomly varies the direction of rotation from one shaft to the other. In DRP, both parameters, direction of rotation, and angular velocity are randomized across the different shafts. Compared to SP and SRP, DRP is known to generate a more isotropic homogenous turbulent flow with higher levels of turbulence intensities [35].

A Nortek Vectrino + acoustic Doppler velocimeter (ADV) with a measurement accuracy of ± 0.005 m/s was used to perform all flow velocity measurements reported in this paper. A 50Hz sampling rate, $1.7 \times 10^{-7} \mathrm{m}^3$ sampling volume, and $120 \mathrm{s}$ sampling duration [4] were maintained across all flow measurements. The phase space thresholding (PST) technique developed by Goring and Nikora [36] was employed to eliminate the spikes observed in the measured velocity-time traces; the spikes identified were replaced with the mean velocity calculated from the time trace. In accordance to Reynolds decomposition, the velocity component u(t) (also v(t) and w(t)) can be broken down as follows

$$u(t) = U + u'(t) \tag{1}$$

into U, the time-averaged component, and u'(t) the time-dependent fluctuating component. The streamwise turbulence

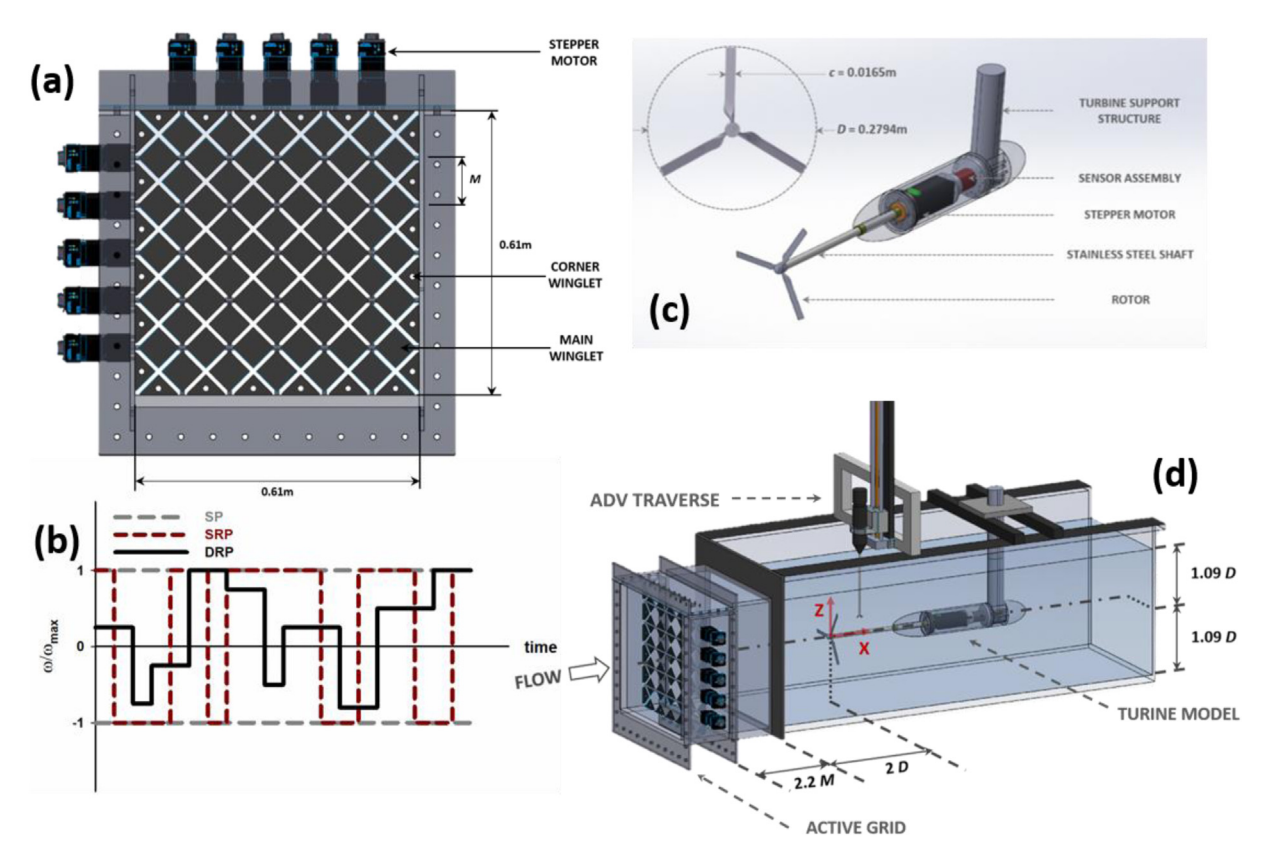


Fig. 1. Schematic of (a) active grid turbulence generator, (b) forcing protocols utilized to operate the active grid (ω is winglet shaft angular velocity in radians/s) (c) 1:20 scale tidal turbine model used in the current study, (d) experimental arrangement with the 5-shaft configuration of the Active Grid.

intensity Ti, and non-dimensional Reynolds stress component R_{XZ} , are estimated as follows [5,37].

$$T_i = 100 \frac{\sigma(u)}{U_{\infty}} \tag{2}$$

$$R_{XZ} = \frac{1}{U_{\infty}} \sqrt{\left| \frac{1}{N} \sum_{i=1}^{N} u_i' w_i' \right|}$$
 (3)

where $\sigma(u)$ is the standard deviation of the collected velocity samples, U_{∞} is the time-averaged inflow velocity at that particular depth-wise location to account for the effects of inflow velocity shear, N is the total number of velocity samples taken, and T is the sampling duration. The auto-covariance function R(s) and the integral length scale L are defined as shown below [37]; s represents the time lag.

$$L = U \int_{0}^{T} \frac{R(s)}{R(0)} ds \tag{4}$$

$$R(s) = \langle u'(t)u'(t+s)\rangle \tag{5}$$

2.2. Tidal turbine model description and performance metrics

A 1:20 scale, three-bladed tidal turbine model was tested in the current work. The 0.279m diameter (D) rotor was made of constant chord (c = 0.016m), no twist, SG6043 profiled blades [4,9,10] (see Fig. 1c for schematic). With a rotor area of 0.061 m², the turbine

model operated at a blockage ratio (rotor area/cross-section of the test section) of 16% while operating in the T³F facility at Lehigh University. A stepper motor identical to the one employed in the active grid turbulence generator was used for the precise control of rotor shaft rotational speeds. The loads experienced by the rotor were measured using a sensor assembly placed within the nacelle; the sensor assembly was primarily a combination of a thrust (Interface, Model# SML-25) and a torque sensor (Interface, Model# MRT2P) configured to decouple and separately evaluate the force components acting on the turbine rotor. The manufacturer prescribed non-repeatability of the two sensors were ±0.0334N and ±0.001Nm, respectively, and were more sensitive than the load cells utilized in some of the previous experimental measurements reported by the authors [10,38]. The turbine nacelle was maintained pressurized (~20 kPa gauge pressure) to avoid water ingress and damage to the stepper motor and sensor assembly. In all measurements involving the turbine, the rotor was placed at a downstream distance of two diameters (2D) from the test section entrance [4], unless mentioned otherwise. The torque (0) and thrust (T) loads experienced by the rotor were captured at a sampling rate of 200 Hz for a period of 120 s [4]. In order to capture the total kinetic energy flux in the turbine rotor area and obtain a more representative estimate of the turbine performance, a method proposed by Wagner et al. [29] is used. The rotor is area is broken down into 0.5" tall segments (resulting in a total number of segments, n = 23), each with a representative inflow velocity (U_i) and a corresponding area (A_i) . The total kinetic energy influx into the rotor area therefore can be obtained using the following expression

$$KE_{in} = \frac{1}{2} \sum_{i=1}^{n} A_i U_i^3 \tag{6}$$

An equivalent flow velocity U_{eq} representative of the total kinetic energy influx into the rotor plane is estimated using eq (7) and is subsequently used for evaluating the non-dimensional performance coefficient, power coefficient (C_P), thrust coefficient (C_T), and tip speed ratio (TSR) defined in Eq. (8).

$$U_{eq} = \left(\frac{1}{A} \sum_{i=1}^{n} A_i U_i^3\right)^{\frac{1}{3}} \tag{7}$$

$$C_p = \frac{Q\Omega}{\frac{1}{2}\rho A U_{eq}^3} , \quad C_T = \frac{T}{\frac{1}{2}\rho A U_{eq}^2} , \quad TSR = \frac{R\Omega}{U_{eq}}$$
 (8)

where A is the rotor area (m²), Ω is the rotor angular velocity (rad/s), and ρ is the water density (kg/m³). The method detailed in the work of Bahaj et al. [39] was utilized to blockage correct calculated non-dimensional performance coefficients.

3. Results & discussion

The different inflow conditions generated in the water tunnel using the active grid and its effects on performance coefficients and near-wake flow features of the tidal turbine model are discussed in this section. All experiments presented in the current work were carried out at inflow velocities higher than 0.82 m/s, as Reynolds number effects on the turbine model used were found to minimal beyond 0.82 m/s [38]. To minimize blockage due to the active grid at such high flow velocities, the 5-shaft configuration (horizontal shafts only) was adopted in this study (see Fig. 1d for a schematic of the experimental arrangement in the T³F; Fig. 2a depicts the 5-shaft configuration of the active grid).

3.1. Characterizing the inflow conditions

Four distinct inflow conditions were tested in the experiments; a homogeneous quasi-laminar flow obtained without the use of active grid (baseline laminar flow with a nominal Ti), a homogenous turbulent inflow referred to as Elevated Ti generated with the active grid installed and operating in the double random forcing protocol (3.14 radians/sec was set as the maximum angular velocity (ω_{max}) attainable by the winglet shafts), and two sheared turbulent inflows, named low-shear and high-shear generated using static mode operation of the active grid. For the sheared inflows, the winglet shafts were oriented in a manner such that the blockage due to the winglet shafts varied gradually from their highest value at the bottom-most shaft (winglets perpendicular to the flow) to its least value at the top-most shaft (winglets parallel to the flow). The angular positions of the shafts, numbered #1 (top-most shaft) - #5 (bottom-most shaft) with respect to the direction of flow in the tunnel, are listed in Table 1. Fig. 2a illustrates the 5-shaft configuration of the active grid and a schematic describing the angle θ listed in Table 1 between the flow direction in the tunnel and the winglet shafts. The depth-wise variation of U and Ti measured in the water tunnel test section for the four different inflows are presented in Fig. 2b-c. The homogenous inflow cases can be seen to have a near-uniform inflow velocity; U averaged across the rotor depth was estimated to be 0.82 m/s in the quasi-laminar flow and 0.83 m/s in the elevated Ti case. The deviations in mean velocity for the two cases were restricted to values < 2% of the depth-averaged mean except at Z/D > 0.45 in the elevated *Ti* case, where it reached values as high as ~5%. Similar to *U*, the depth-wise variation in *Ti* for the homogenous inflow cases were also found to be minimal; for the two cases, Ti across the depth of the rotor was found to remain contained within 2.8 \pm 0.4% and 13 \pm 0.7%, respectively. The sheared-turbulent inflows, on the other hand, were devised to have

a significant depth-wise variation of *U* and *Ti*. For the low-shear case, U varied from a value of ~0.7 m/s at the bottom end of the rotor to ~1 m/s at the top end of the rotor, and *Ti* varied from a value of ~15% at the bottom end of the rotor to ~4% at the top end of the rotor. The range of variation of *U* in the high-shear case was comparable to the low shear case: however, the variation in Ti was considerably larger: in the high-shear case. Ti varied from a value of ~25% at the bottom end of the rotor to ~6% at the top end of the rotor. While the quasi laminar, elevated Ti, and low shear cases were developed at a downstream distance of 2D from the active grid, the high-shear inflow profile was developed at an upstream location of 0.5D from the test section entrance. The depth-wise fluctuations observable in the high-shear case are a consequence of the upstream location that makes flow characteristics comparatively less homogenous owing to the proximity to the turbulence generator.

To better compare the sheared turbulent inflows to the homogenous inflow cases, the depth-wise variability of U and Ti across the rotor can be described as 0.85 ± 0.15 m/s and $9.5 \pm 5.5\%$ for the low-shear case and 0.88 ± 0.18 m/s and $16 \pm 11\%$ for the high-shear case.

Also, the velocity shear corresponding to the two cases can be described as

$$U(z) = U_{hub} \left(\frac{z}{z_{hub}}\right)^n \tag{9}$$

where U_{Hub} is the streamwise velocity measured at hub height, and z_{hub} is the height of the hub from the bottom of the tunnel. The shear exponent n for the low-shear and high-shear cases was estimated to be 0.28 and 0.44, respectively. By comparing the nvalues to some of the available field measurements [40], it can be seen that the sheared flows generated within our T³F are well representative of flow conditions at potential tidal energy sites with the low shear case (n = 0.28) similar to values measured at tidal energy sites for flood tides and the high shear case (n = 0.44) on the higher side of values measured for ebb tides. The characteristics parameters for all the inflow conditions tested are summarized in Table 2. To accurately account for the inflow impinging on the turbine, the rotor was always positioned at the same location at which the different inflow conditions were devised, i.e., the rotor was placed at a downstream location of X/D = 2 when tested in the quasi laminar, elevated Ti and low shear inflows and at X/D = 0.5when tested in the high shear inflow.

The power spectral density (PSD) (measured at the rotor plane location in the absence of the rotor) for the four inflow cases is shown in Fig. 3. Two locations along the depth of the test section are considered: Z/D = 0.5 (top end of the rotor) and -0.5 (bottom end of the rotor). The spectra presented clearly reflect the variations in energy distribution across the different scales present in the tested inflows. The homogenous inflow cases can be observed to have a near-identical spectra at the two locations considered; the -5/3 decay slope commonly noted in the inertial subrange can be identified in the elevated Ti case. The low-shear and high-shear cases, on the other hand, evidently display a depth-wise variation in the energy content of its constituent scales. Correlated with the depth-wise increase in turbulence intensity, the turbulent energy contained within the range of scales in the inflow was observed to increase with depth in the water channel. From the two locations presented, the energy content of scales in the sheared turbulent inflow can be seen to be higher at the location of Z/D = -0.5, which is the lowest depth-wise location plotted; at this location, a -5/3slope is noticeable in the inertial subrange.

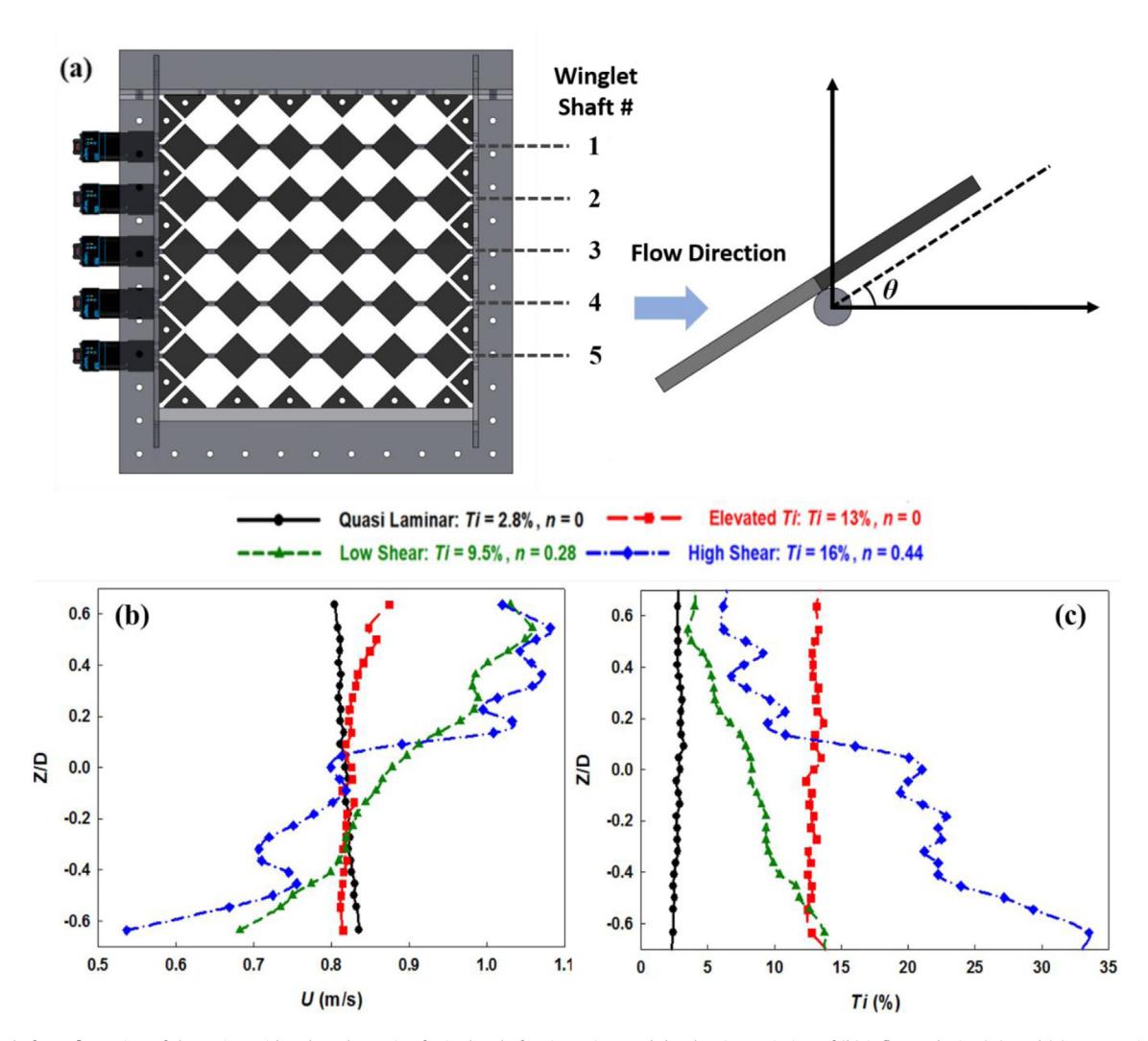


Fig. 2. (a) 5 shaft configuration of the active grid and a schematic of winglet shaft orientation, and depth-wise variation of (b) inflow velocity (*U*), and (c) streamwise turbulence intensity (*Ti*).

Table 1The angular orientation of horizontal shafts used to generate the Low-shear and High-shear inflow cases (also see Fig. 2a).

Shaft #	Angular Position (θ) with respect to the flow direction		
	Low-shear case	High-shear case	
1	0	0	
2	11.25	28.125	
3	-22.5	-22.5	
4	-112.5	-101.25	
5	-90	-90	

Table 2Characteristic parameters for the different inflows tested.

Case	U (m/s)	Ti (%)	L(averaged)	n
Quasi Laminar	0.82 ± 0.012	2.8 ± 0.4	0.8D	0
Elevated Ti	0.83 ± 0.03	13 ± 0.7	0.4D	0
Low Shear	0.85 ± 0.15	9.5 ± 5.5	0.09D	0.28
High Shear	0.88 ± 0.18	16 ± 11	0.15D	0.44

3.2. Turbine performance characteristics

3.2.1. Power and thrust coefficient

The performance coefficients of the turbine model evaluated for all four inflow conditions are plotted in Fig. 4a and b. Each data point was measured three times, and the mean of the three measurements is plotted in the figure; the error bars included denote the 95% confidence interval. Similar to the observations reported in the literature with regards to homogenous inflow turbulence [5,6], sheared turbulent inflows too were not found to have a significant impact on the estimated C_P values.

As can be seen in Fig. 4a, the C_P curves obtained for the different inflows can be seen to be comparable to each other (within the variability in the measurement) at TSR's < 3. The differences between the tested cases become more identifiable in the operating range beyond a $TSR \sim 3$. Like the homogenous elevated Ti case, both the sheared turbulent inflows result in a reduced maximum C_P despite the increased corresponding inflow velocities. The maximum C_P obtained in the high shear flow (n = 0.44) was comparable to the maximum C_P observed in the elevated Ti case and was $\sim 5\%$ lower than the max C_P obtained in the quasi-laminar

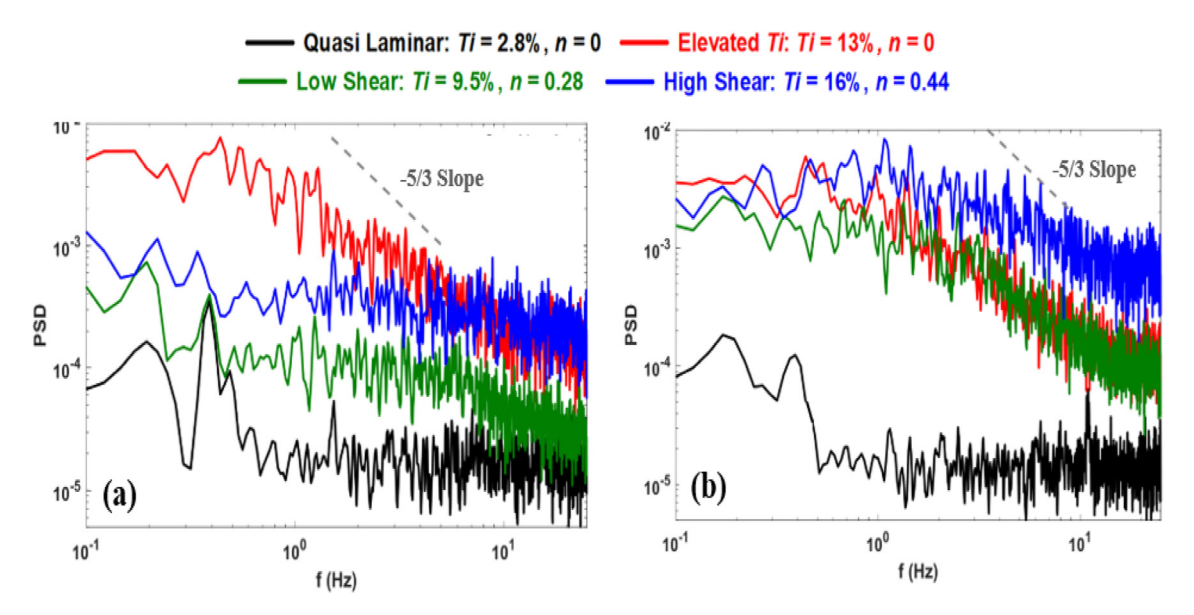


Fig. 3. Inflow power spectral density at the rotor plane at depth-wise locations (a) Y/D of 0.5, (b) Y/D of -0.5.

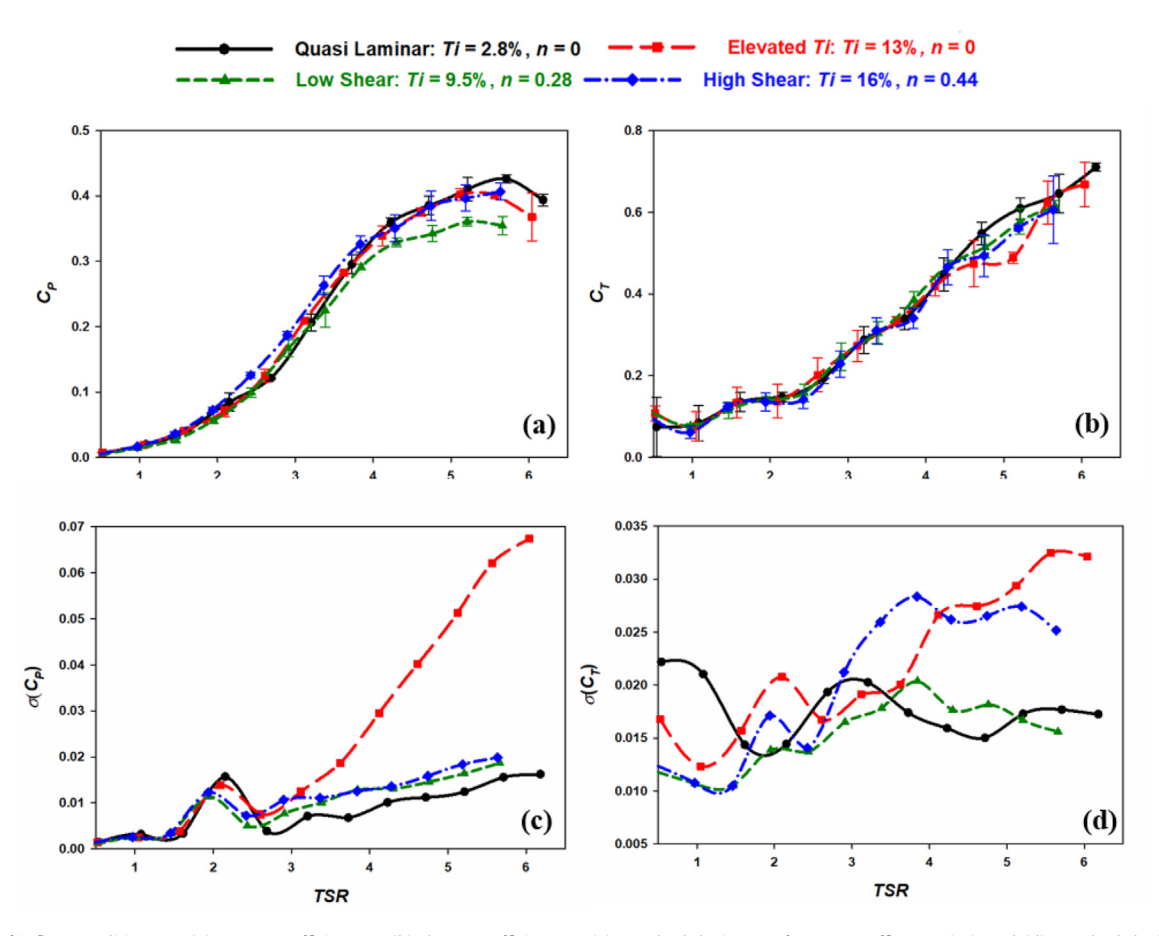


Fig. 4. Effect of inflow conditions on (a) power coefficient, C_P (b) thrust coefficient, C_T (c) standard deviation of power coefficient $\sigma(C_P)$, and (d) standard deviation of thrust coefficient, $\sigma(C_T)$.

flow. Interestingly, the C_P values measured in the low shear inflow (n=0.28) were consistently lower in the operating range; the maximum C_P in the low shear case was ~15% lower in comparison to the quasi-laminar case. In all four cases, the maximum C_P was observed to lie within 5<*TSR*<6, with the quasi laminar flow

resulting in the maximum C_P (~0.42) at a TSR of 5.9, higher compared to the turbulent inflow cases. The effect of the inflow profile on the time-averaged C_T is shown in Fig. 4b. The C_T curves can be seen to collapse better than the C_P curves, especially at TSR<3. The differences between the curves are most noticeable

within 5 < TSR < 5.5, where C_T measured in the elevated Ti case was the least and was 20% lower compared to the C_P measured in the quasi-laminar case.

3.2.2. Load fluctuations on the rotor

The load fluctuations experienced by the rotor are quantified in terms of the standard deviations of the non-dimensional performance coefficients, $\sigma(C_P)$, and $\sigma(C_T)$ (see Fig. 4 c,d). Relative to C_P $\sigma(C_P)$ is noticeably more sensitive to variations in the inflow at TSR > 2.5. $\sigma(C_P)$ values estimated in elevated Ti were observed to increase significantly with TSR, reaching a value 4.5 times larger than the corresponding value in the quasi-laminar flow at the maximum TSR tested. Though not as high in comparison to elevated Ti case, $\sigma(C_P)$ estimated in the sheared turbulent inflows was observed to be larger (~30% within 3<TSR<5.7) than its counterparts in the quasi-laminar inflow. It is interesting to note that the $\sigma(C_P)$ values estimated in the low-shear and high-shear cases are remarkably similar to each other, except for a negligible increase seen in the high shear case. Intuitively, the high shear case should have resulted in the maximum fluctuations of all cases. This observation is conjectured to be an artifact of the rotor averaged nature of the measured loads. The sensor assembly used in the model is essentially set up to capture the loads experienced by the turbine shaft and not the individual blades. Therefore, the captured instantaneous loads are not likely to reflect the extent of load variability experience by the individual blades. Similar to $\sigma(C_P)$, $\sigma(C_T)$ values were more sensitive to the variability in inflow profile than C_T . $\sigma(C_T)$ in the elevated *Ti* case increased with *TSR*, reaching values 2.7 times larger than the corresponding values at TSR ~6 in the baseline quasi-laminar flow. Also, the increase in $\sigma(C_T)$ in the high-shear inflow was significant, reaching values ~1.5 times larger than its counterparts in the quasi-laminar flow. $\sigma(C_T)$ estimated in the low-shear inflow, on the other hand, was more comparable to the values observed in the quasi-laminar inflow; the maximum increase in $\sigma(C_T)$ measured in the low-shear inflow for the turbine operating range was noted to be ~30% when compared to the corresponding value in the quasi-laminar flow and was observed at a TSR = 4. The experimental measurements indicate that rotor thrust and torque fluctuations experienced in sheared turbulent inflows show the tendency to scale with the depth-averaged value of turbulence intensity across the rotor. This effect is more pronounced in the case of $\sigma(C_T)$. Such load fluctuations can have a significant impact on the design requirements for the different turbine components and their operational life. Therefore, they must be estimated and accounted for in the design phase itself to produce robust and efficient turbine systems [6].

3.3. Rotor wake characteristics

3.3.1. Wake velocity deficit

All wake flow parameters presented in the current work were evaluated at the optimal TSR of 4.8. The authors would like to point out that the presented wake profiles are missing data points close to the center of the domain solely because the center locations were inaccessible for measurement due to the turbine shaft at X/D = 0.5 and the turbine body at X/D = 2. The wake velocity deficit, U^* is a non-dimensional parameter that characterizes the drop in streamwise velocities due to energy extraction by the rotor. It is defined as

$$U^{*}(Y,Z) = \frac{U(Y,Z) - U_{WAKE}(Y,Z)}{U(Y,Z)}$$
(10)

where $U_{WAKE}(Y, Z)$ is the time-averaged streamwise velocity at a particular depth-wise location in the wake, and U(Y, Z) is the

corresponding time-averaged inflow velocity value. U^* profiles at the downstream locations, X/D=0.5, 2 are plotted in Fig. 5. A slow-moving wake with a width close to the diameter of the rotor and a region of flow acceleration around the rotor (due to blockage effects) can be identified in all four cases. At the closer downstream location of X/D=0.5, all four inflow cases can be seen to incite a U^* profile resembling a top-hat, characteristic of a near-wake region that has been minimally impacted by momentum diffusion from the ambient flow. A region of faster moving flow (lower U^*) can be noticed within -0.3 < Z/D < 0.3; this observation is conjectured to be a consequence of the rotor design used in the current work [44–46]. The reduced thickness at the root of the turbine blades (owing to the type of blade attachment incorporated, see Fig. 1c is hypothesized to result in a lower hindrance to the incoming flow, inducing a noticeable local acceleration of the streamwise velocity component.

The maximum velocity deficit measured at X/D = 0.5(~0.45–0.50) was found to be comparable for the four different inflows. While the wake U^* profiles corresponding to the quasilaminar and elevated Ti cases are appreciably symmetric about the turbine axis, asymmetry is observable in the U^* profiles corresponding to the low-shear and high-shear inflows, especially in terms of the flow acceleration around the rotor; the acceleration at Z/D = 0.63 was lower than the acceleration at Z/D = -0.63 by 70% in the low shear flow and 90% in the high shear flow. Wake reenergization was clearly noticeable with the downstream propagation of the wake; by X/D = 2, maximum U^* corresponding to the quasi-laminar and elevated Ti cases dropped by ~10% and ~15%, respectively. The effect of inflow shear became more noticeable within the rotor wake with downstream propagation. By X/D = 2, the U* values in the upper half of the rotor wake had evolved to larger values in comparison to their counterparts in the lower half. In other words, U* values in the lower half of the rotor wake dropped considerably faster compared to the velocity deficit values in the upper half. This trend can be correlated to the effect of ambient turbulence. The lower wake, being in a more turbulent environment, undergoes a quicker re-energization in comparison to the upper wake, which is in a less turbulent environment. The maximum velocity deficit in the lower half in both low-shear and high-shear inflows was found to be as much as ~20% lower than the corresponding value in the upper half. Being sufficiently away from the rotor, the increase in streamwise velocity noted in regions close to the rotor hub at X/D = 0.5 was no longer identifiable at X/D = 2.

3.3.2. Wake rotation

The depth-wise variation of the tangential velocity component (V) in the rotor wake is plotted in Fig. 6. It is worthwhile to note that the tangential flow pattern in the wake of the rotor closely resembles that of a Rankine vortex, similar to flow patterns observed in atmospheric phenomena such as hurricanes [41]. A Rankine vortex is a combination of a rigid body vortex and a free vortex; the rigid body vortex (velocity magnitude increasing with distance from the center) manifests in the core region where the radial distance from the center is <R, whereas a free vortex (velocity magnitude decreasing with distance from the center) forms at radial distance > R. It can be observed that at X/D = 0.5, for all four inflow cases, the maximum magnitude of V is larger in the lower half of the wake when compared to the upper half and is hypothesized to be a consequence of the differences in the top/bottom boundary of the water tunnel test section; the lower tip of the rotor is closer to the wall of the tunnel, whereas the upper tip of the rotor is closer to the free surface. The influence of inflow turbulence is also noticeable (for the most part) in the maximum magnitude of V velocity components. Due to the disruptive nature of ambient turbulence, the higher the level of turbulence, the lower the

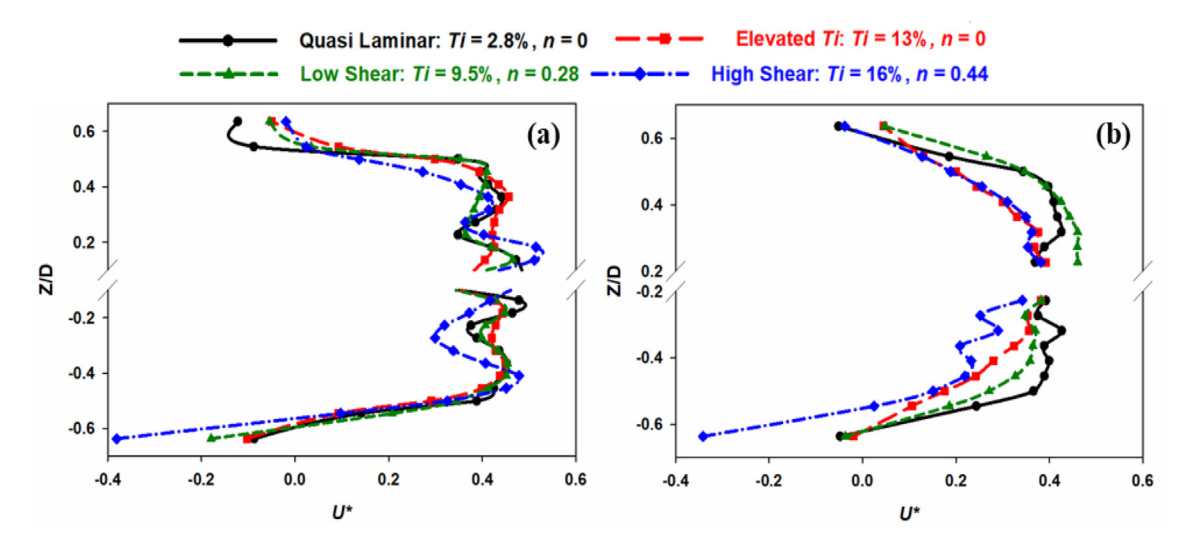


Fig. 5. Depth-wise variation of velocity deficit U^* at downstream locations, (a) X/D of 0.5, (b) X/D of 2.

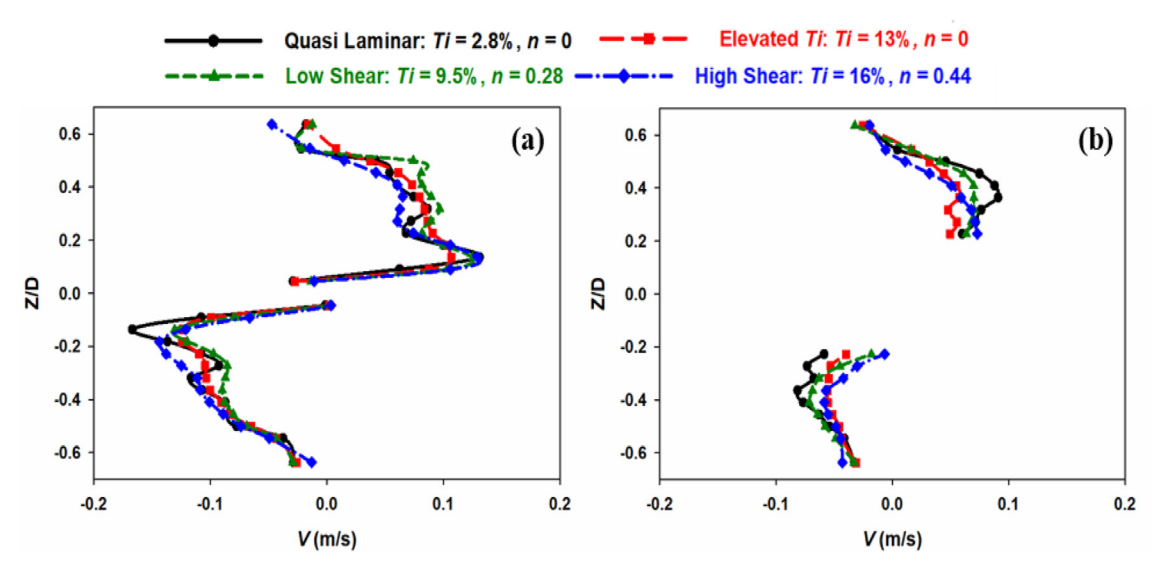


Fig. 6. Depth-wise variation of tangential velocity V at downstream locations (a) X/D of 0.5, (b) X/D of 2.

corresponding maximum tangential velocity. The influence of inflow shear in inducing asymmetry in the wake was not distinguishable at X/D = 0.5 due to the presence of the asymmetry induced by the tunnel boundary effects. This effect (asymmetry due to tunnel boundary conditions) was observed to diminish considerably with downstream evolution of the wake, and the effects of inflow shear became more evident. At X/D = 2, magnitudes of Vacross the depth of the wake were found to scale with the depthwise inflow Ti value; the highest velocities were observed in the guasi-laminar flow, followed by the low shear case. The elevated Ti and high shear cases resulted in comparatively lower tangential velocities; the elevated Ti case led to marginally larger V velocities in the bottom half of the wake, whereas the high shear case lead to marginally larger V velocities in the upper half of the wake correlating with the depth-wise variation in inflow Ti (see Fig. 6b).

The swirl number S (defined below) was evaluated to better characterize the momentum distribution in the wake [42,43].

$$S = \frac{G_{\varphi}}{G_{x}r}, \text{ where}$$

$$G_{\varphi} = \int_{0}^{R} (wr)\rho u 2\pi r dr , \text{ and}$$

$$G_{x} = \int_{0}^{R} u\rho u 2\pi r dr$$

$$(11)$$

Table 3Swirl numbers calculated in the turbine wake for different inflow conditions.

X/D	S	Quasi-Laminar Flow	Elevated Ti	Low Shear	High Shear
0.5	S _U	0.09	0.10	0.10	0.05
	$S_{\rm B}$	0.14	0.13	0.12	0.15
2	$S_{\rm U}$	0.12	0.06	0.08	0.05
	$S_{\rm B}$	0.10	0.07	0.09	0.07

where G_{ω} is the axial flux of angular momentum and G_{x} is the axial flux of linear momentum. To capture the differences between the upper and lower halves of the wake, the definite integral in eq. (11) was carried out for two distinct depth-wise distance ranges at a particular downstream location. The swirl number S_{II} representative of the upper half of the wake was obtained by integrating eq. (11) over the range $0 \rightarrow R_U$, where $R_U = Z/D = 0.5$. Similarly, swirl number S_R representative of the lower half of the wake was obtained by integrating eq (11) over the range $0 \rightarrow R_B$, where $R_B = Z/$ D = -0.5. The swirl numbers thus calculated under the different inflow conditions are listed in Table 3. From the table, it can be seen that S_U values estimated at X/D = 0.5 are consistently smaller than their S_B counterparts; as pointed out earlier in the discussion, this disparity is conjectured to be a consequence of the boundary effects in the water tunnel test section. S_U and S_B estimate obtained in the quasi-laminar elevated Ti and low-shear cases inflows were considerably close to each other at X/D = 0.5. On the other hand, S_U and S_B estimates obtained in the high-shear inflow were significantly different from their counterparts in the other three inflows; S_B in the high shear inflow was ~2.8 times the corresponding S_U and was 11% larger than S_B estimated in the quasilaminar flow. With downstream travel, the disparity between S_U and S_R estimates for the different flows can be observed to decrease. As in the case of tangential velocity components, the averaged swirl number at X/D = 2 was observed to scale with the depth-averaged inflow turbulence intensity. The averaged swirl numbers calculated in the low-shear, elevated Ti and high-shear cases were lower than the averaged swirl number estimated in the quasi-laminar flow by 21%, 40%, and 48%, respectively, clearly illustrating the disruption to wake rotation caused in higher ambient turbulence. In the current work, swirl numbers were not estimated beyond a downstream distance of X/D = 2 owing to turbine support structure interference and limitations of water tunnel test section length.

3.3.3. Streamwise turbulence intensity

Profiles of streamwise turbulence intensity, Ti, in the rotor wake are plotted in Fig. 7. At X/D = 0.5, a gradual rise of Ti in regions close to the hub and Ti peaks close to the rotor tips are observable in all inflow conditions. In the elevated Ti case, Ti measured in the wake was symmetric about the turbine axis and was higher than the Ti values in the quasi-laminar and low-shear cases; Ti measured at the

peaks near the rotor tip were found to be as high as ~21%, and in the annular intermediate region between the rotor tip and hub was found to be in the 11-15% range. An asymmetric character was evident in the wake Ti profile corresponding to the sheared inflow cases. For the low-shear profile, Ti estimated near the bottom edge of the wake (in the more turbulent inflow) was found to be ~28% higher than Ti estimated at the top edge of the wake. Ti in the lower intermediate region (9–10%) can also be observed to be larger than its counterparts in the upper intermediate region (5-7%). The asymmetry in high-shear inflow was even more significant; Ti values estimated close to the bottom edge of the wake were 70% higher than values estimated at the upper edge. Ti in the lower intermediate region (13-16%) can also be seen to be considerably larger than the Ti values in the upper intermediate regions (8–10%). A correlation to the depth-wise variation in inflow Ti values is clearly observable in all the different cases; the higher the inflow Ti at a particular depth-wise location, the higher the Ti at the corresponding wake location. The only notable exception to this trend was the Ti peaks close to the rotor tips in the quasi-laminar inflow; the upper tip closer to the free surface was considerably more turbulent, reaching values of Ti close to 15%, whereas the lower peak close to the tunnel floor was contained slightly below a value of Ti = 9%. The magnitudes of Ti in the wake in elevated Ti and sheared inflows were observed to drop with the downstream propagation of the wake (see Fig. 7b).

At X/D=2, Ti values corresponding to the elevated Ti case drop to values in the 10-16% range, and the same in the low-shear and high-shear inflows drop to an even lower, 5-15% and 6-16% range, respectively. The asymmetric character of the sheared inflows is still evident at X/D=2; the Ti peak close to the lower tip of the rotor in the low-shear and high-shear inflows remained ~22% and ~68% higher (respectively) than the peak at the upper tip of the rotor. The turbulence in the lower intermediate region was also noticeably higher. The Ti profile in the quasi-laminar flow was noticeably less diffused. Local spikes in Ti ranging in values between 11 and 13% were discernible at X/D=2. However, the asymmetry in the magnitudes of peaks close to the rotor tip was found to be reduced; the peaks were comparable with Ti values in the 11-13% range.

3.3.4. Reynolds stresses

Fig. 8 plots the Reynolds stress component R_{XZ} at X/D = 0.5, 2. Similar to the trends observed in wake T_i , R_{XZ} peaks can be observed

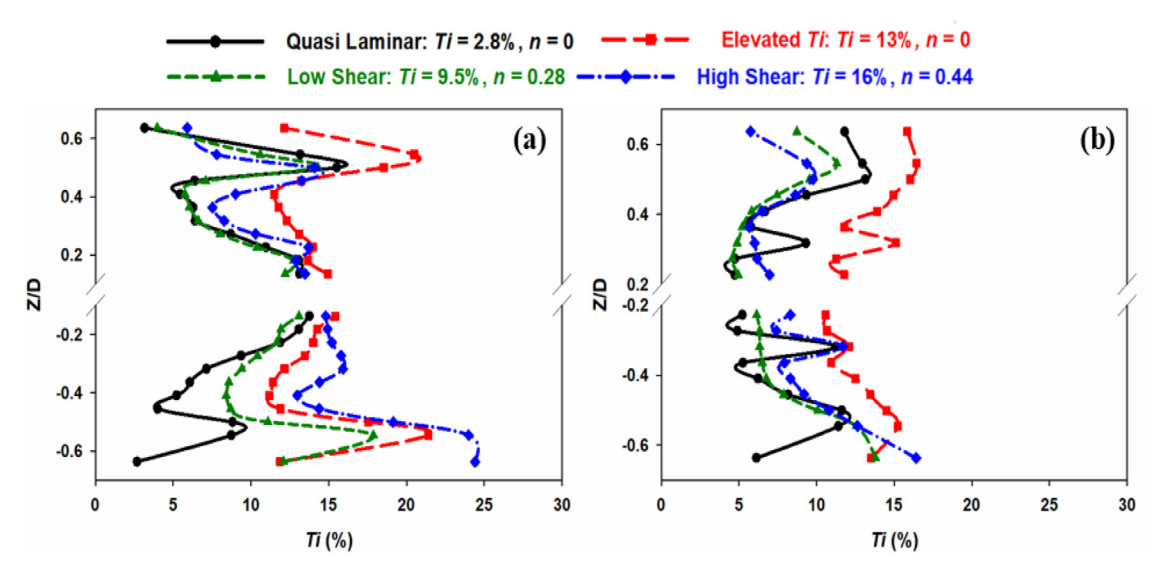


Fig. 7. Depth-wise variation of streamwise turbulence intensity Ti, at downstream locations (a) X/D of 0.5, (b) X/D of 2.

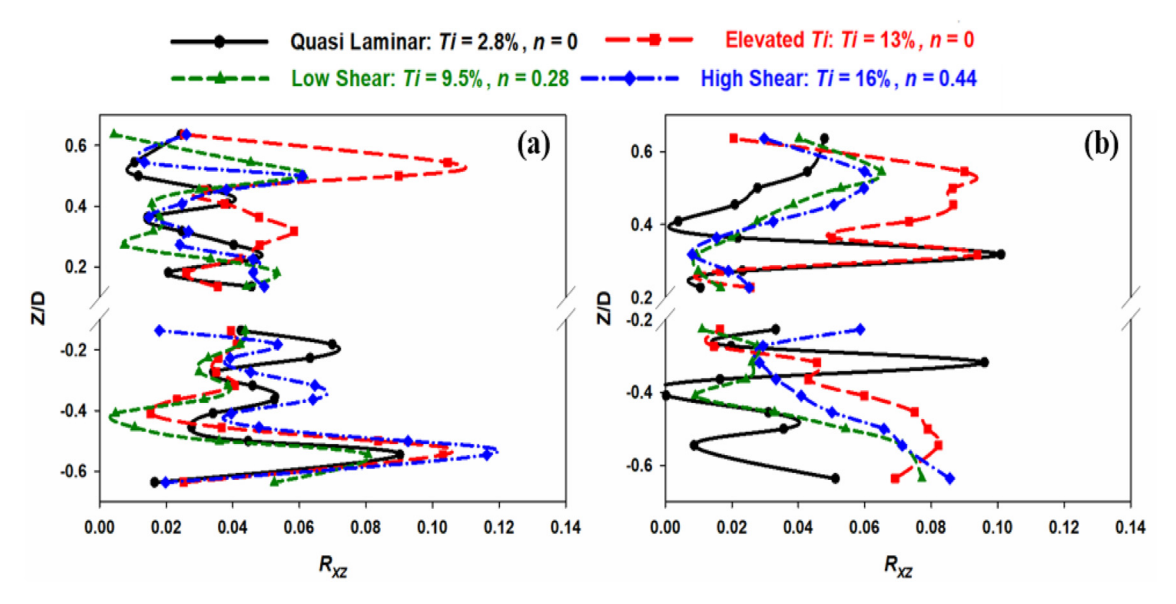


Fig. 8. Depth-wise variation of R_{XZ} Reynolds stresses at downstream locations, (a) X/D of 0.5, (b) X/D of 2.

at the wake edges, further emphasizing the role of the shear layer in the production of turbulence in the rotor wake. The symmetric nature of the elevated Ti case and the asymmetric nature of sheared inflows are reflected in the depth-wise R_{XZ} profiles as well, specifically in terms of the maximum R_{XZ} values observed in the peaks close to the rotor tips. In the elevated Ti case, the peaks were comparable with a magnitude of $R_{XZ} = \sim 0.10$; in the sheared inflow cases, on the other hand, the peak in the lower half of the wake was larger than its upper wake counterpart by $\sim 33\%$ in the low-shear case and $\sim 90\%$ in the high-shear case. Considerable depth-wise variation/fluctuation of R_{XZ} in the intermediate regions was noticeable in all the inflow conditions tested.

Further downstream at X/D = 2, the R_{XZ} profiles corresponding to the elevated Ti and sheared inflow cases become more diffused with noticeably lower fluctuations in the intermediate regions. Large values persist in regions close to the rotor tip; however, they can be observed to be less concentrated at the rotor tips, suggesting

intense mixing over larger portions of the wake. The asymmetric nature incited by the sheared inflows can be observed at X/D=2 as well, via the larger stresses observed in the lower half of the rotor. Unlike the turbulent inflow cases, the stresses in the quasi-laminar inflow were found to increase at X/D=2, reaching higher values compared to the values observed in the turbulent inflows. This observation is in alignment with findings reported in the literature, which illustrate that, at low levels of freestream turbulence, wake mixing intensifies with downstream propagation and peaks within the 5-7D downstream range [6].

3.3.5. Integral length scales

The evolution of integral length scales L, in the wake of the rotor, is illustrated in Fig. 9. It can be seen that the depth-wise profile of L in the wake of the rotor is notably affected by the inflow characteristics. At X/D = 0.5 in the quasi-laminar inflow, L was found to be appreciably uniform across the wake with values in the

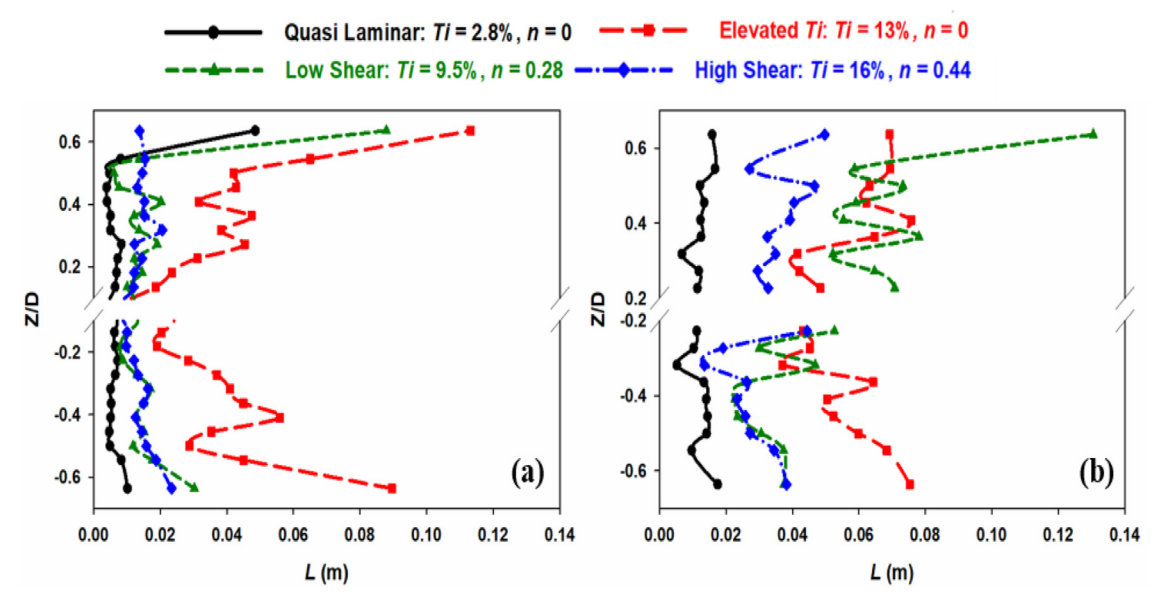


Fig. 9. Depth-wise variation of integral length scales L at downstream locations (a) X/D of 0.5, (b) X/D of 2.

0.0038m-0.0063m range. Although, to a smaller extent, depthwise uniformity was also observable in the sheared inflow cases with L varying in the 0.0076m-0.0203m range for the low-shear case and 0.0004m-0.0207m range for the high-shear case. On the contrary, elevated Ti case resulted in a noticeably larger and non-uniform depth-wise variation of L (0.0102m-0.0635m) at X/D = 0.5. L estimated in the regions close to the rotor hub, and tip showed the tendency to be smaller than the values calculated in the intermediate regions. With downstream propagation, the integral length scales were found to become larger in all four tested cases (see Fig. 9b). At X/D = 2, L across the wake in the quasi-laminar inflow remained fairly uniform in the 0.0051m-0.0127m range, and the depth-wise variability of L in the elevated Ti case was found to remain contained within the 0.0381m-0.0762m range. In the sheared turbulent inflows, unlike the symmetric profile observed at X/D = 0.5, an asymmetric L profile is noticeable at X/D = 2, with L showing the tendency to increase with distance from the bottom of the tunnel. This observation is hypothesized to be a consequence of the stretching experienced with an increase in flow velocity with an increase in distance from the bottom of the tunnel. Also, the size (or growth) of the integral length scales observed at X/D = 2 can be correlated to the averaged L of the turbulent inflows; the largest inflow integral length scale was evaluated in the elevated Ti case followed by the low-shear and high-shear cases in order. The large averaged L estimated at X/D = 0 in the quasi-laminar inflow is more of an artifact of the longer time correlations expected in a near laminar flow and therefore is not considered representative of large inflow structures.

3.3.6. Wake spectra

The spectral characteristics of the rotor wake were also explored to examine the impact of inflow characteristics on the propagation

of flow periodicities (such as tip vortices) incited by the rotor. In addition to the load fluctuations caused by inflow turbulence, exposure to such inflow periodicities can strain downstream turbines from a fatigue perspective and could compel frequent maintenance procedures escalating the cost of energy produced by the technology. Fig. 10 illustrates the frequency spectra measured at depth-wise locations Z/D = -0.5 and 0.5. at downstream distances X/D = 0.5, 2. At X/D = 0.5, it was observed that the spectra corresponding to the low-shear case at Y/D = 0.5 reflect characteristics very similar to the spectra of the quasi-laminar flow case. The blade passing frequency F_B , which is three times (for a three-bladed turbine), the rotor rotational frequency (F_R) can be clearly identified at this location. F_B can be identified in the high-shear inflow case as well; however, it can be clearly seen to have a lower amplitude in comparison to the guasi-laminar and low-shear inflow cases, owing to the comparatively higher inflow Ti at the chosen depth-wise location. At Z/D = -0.5, the spectra corresponding to the low-shear case had a considerably lower amplitude at F_B ; the frequency component was not discernible in the highshear inflow. This observation emphasizes the immediate impact of sheared-turbulent inflow, illustrating the asymmetric break up of tip vortices in the more turbulent ambient flow region. With the downstream evolution of the wake, a redistribution of spectral energy can be observed in the quasi-laminar inflow case (at X/ D=2), with F_R becoming the more dominant frequency component. At X/D=2, a minor dominance of F_R can be observed at the depth-wise location Z/D = 0.5 for the low-shear inflow case; however, at Y/D = -0.5, the spectrum has no identifiable peaks as in the elevated Ti case. The high-shear inflow case results in no identifiable frequency peaks at both depth-wise locations at X/D = 2. The periodicity evolution trends identified in the case of the sheared-turbulent inflow suggests that while sheared/asymmetric

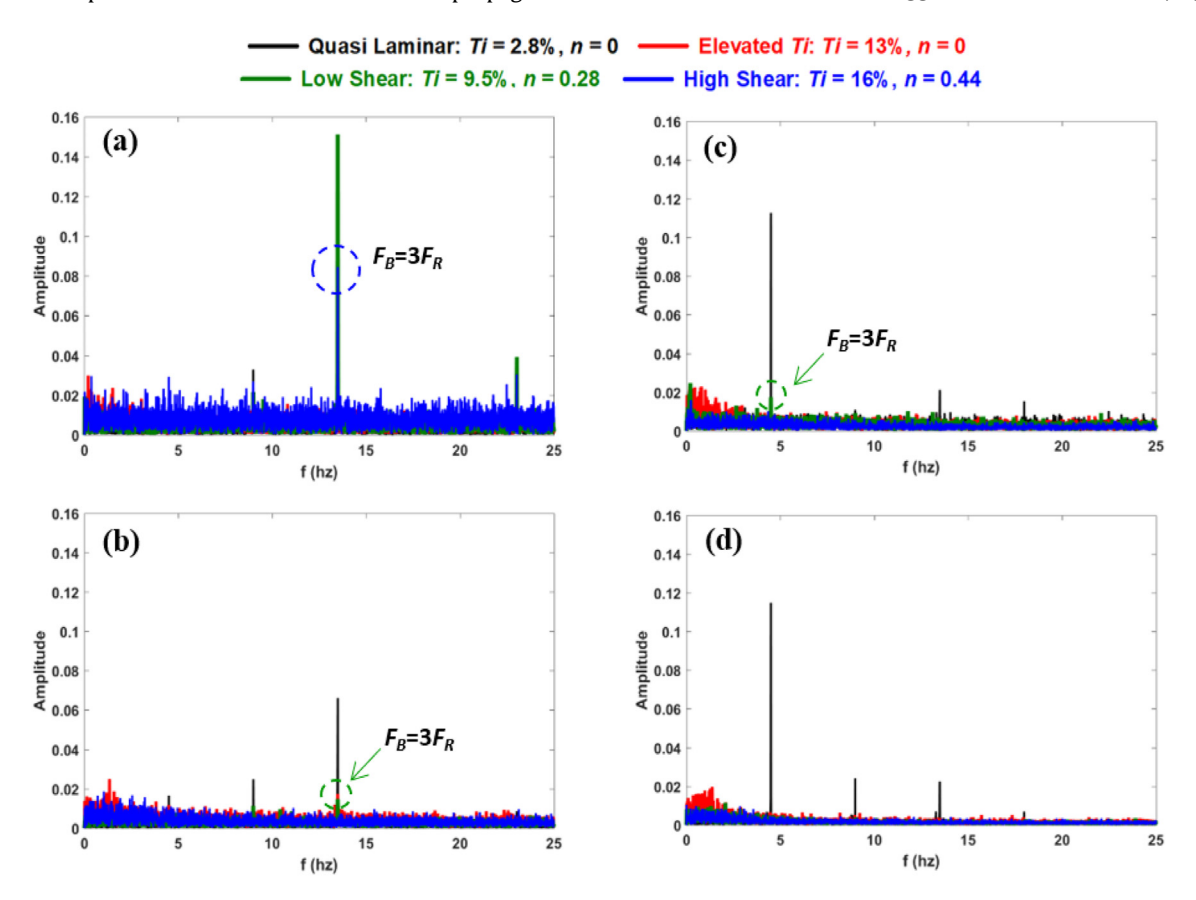


Fig. 10. Frequency spectra estimated in the rotor wake at (a) X/D of 0.5, Y/D of 0.5, Y/D of 0.5, Y/D of 0.5, Y/D of -0.5, (c) X/D of 2, Y/D of 0.5 and (d) X/D of 2, Y/D of -0.5.

turbulent inflow can incite asymmetric spectral characteristics in regions very close to the rotor, downstream evolution of the rotating wake redistributes spectral energy among its frequency components overcoming the influence of ambient flow shear on spectral characteristics.

4. Concluding remarks

The experimental results presented in this paper illustrate the effects of sheared-turbulent inflows on the performance coefficients and near wake flow features of a 1:20 laboratory-scale tidal turbine model. The main findings of the study can be summarized as follows:

- From a performance perspective, the effects of inflow conditions were best reflected in the measured torque and thrust fluctuations. The standard deviations of the experienced turbine loads in the low-shear and high-shear cases were similar to each other and larger than the quasi-laminar inflow by ~30–50%. The corresponding increase in the elevated *Ti* case was significantly larger (torque fluctuations 4.5 times and thrust fluctuations 2.7 times). Inflow turbulence and shear, however, were not found to have a dramatic impact on the time-averaged performance coefficients of the tested tidal turbine model. The maximum *C*_P measured in the high-shear and low-shear inflows were 5% and 15% lower than the maximum *C*_P obtained in the quasi-laminar inflow and was observed at a comparatively lower *TSR*.
- An asymmetric wake character was gradually evident with the downstream evolution of the velocity deficit profile in the sheared-turbulent inflow cases. By X/D = 2, the portion of the wake in the more turbulent inflow region (lower half) showed the tendency to recover streamwise velocities faster than the portion of the wake in the less turbulent region (upper half). The asymmetry was more pronounced in the high-shear case compared to the low-shear case. Swirl number representing the aspect of wake rotation was found to scale with the depth-averaged value of Ti.
- The effect of inflow shear on the measured wake turbulence intensities was found to be more immediate. *Ti* in the lower portion of the wake (from rotor hub to tip) was consistently more than the *Ti* values in the upper portion of the wake starting from *X*/*D* = 0.5 itself. A similar trend was reflected in the measured Reynolds stresses as well. The asymmetry, however, was found to reduce with downstream travel. As in the case of velocity deficit, the asymmetry was more noticeable in the highshear case.
- As observed in the case of wake velocity deficit, the response of integral length scales in the rotor wake to the inflow shear was observed to be more gradual. An asymmetric depth-wise variation of *L* becomes noticeable only at *X*/*D* = 2, with *L* showing the tendency to grow faster with distance from the bottom boundary. The growth of *L* in the wake correlated well to the averaged *L* in the inflow; the high-shear case had smaller *L* values compared to the low-shear case.
- The effect of the sheared-turbulent inflow on wake spectral characteristics was more evident closer to the rotor at X/D=0.5. With downstream travel, a redistribution of spectral energy among frequency components was observed, overcoming the influence of inflow shear.

Inflow variations in the form of freestream turbulence or non-homogeneity/shear would result in variability in the forces experienced by a turbine, thereby resulting in variations in power capture and wake characteristics. The likelihood of wake interaction in

an array configuration further adds a new source of inflow variability to the above problem. As noted in the literature, a clear understanding of the implications of such load/power fluctuations to device survivability and steady electricity generation is vital to developing efficient and robust commercial-scale tidal arrays [23]. The experimental data sets presented in this paper quantify the sensitivity of turbine performance coefficients and near-wake characteristics to a range of controlled inflow turbulence as well as shear and, therefore, would be valuable in calibrating computational models to better predict turbine response and thereby optimize turbine efficiency and the complementing power take-off system. The far-wake implications of inflow shear are beyond the scope of the current work; however, the presented data could be used as a starting point to model such effects.

Declaration of competing interest

The authors declare that they have no known competing financial interests or personal relationships that could have appeared to influence the work reported in this paper.

Acknowledgment

The authors would like to acknowledge the US National Science Foundation (Grant No. 1706358, CBET- Fluid Dynamics) and Lehigh University (through the William G. Harrach and Walker Fellowships) for financial support that has facilitated the research in this publication.

Appendix A. Supplementary data

Supplementary data to this article can be found online at https://doi.org/10.1016/j.renene.2021.05.026.

References

- Z. Zhou, M. Benbouzid, J.-F. Charpentier, F. Scuiller, T. Tang, Developments in large marine current turbine technologies—A review, Renew. Sustain. Energy Rev. 71 (2017) 852–858.
- [2] https://www.verdantpower.com/latest-news.
- [3] S. Chawdhary, C. Hill, X. Yang, M. Guala, D. Corren, J. Colby, F. Sotiropoulos, Wake characteristics of a TriFrame of axial-flow hydrokinetic turbines, Renew. Energy 109 (2017) 332–345.
- [4] A. Vinod, A. Banerjee, Performance and near-wake characterization of a tidal current turbine in elevated levels of free stream turbulence, Appl. Energy 254 (2019) 113639.
- [5] T. Blackmore, L.E. Myers, A.S. Bahaj, Effects of turbulence on tidal turbines: implications to performance, blade loads, and condition monitoring, Int. J. Mar. Energy 14 (2016) 1–26.
- [6] P. Mycek, B. Gaurier, G. Germain, G. Pinon, E. Rivoalen, Experimental study of the turbulence intensity effects on marine current turbines behaviour. Part I: one single turbine, Renew. Energy 66 (2014) 729–746.
- [7] S. Tedds, I. Owen, R. Poole, Near-wake characteristics of a model horizontal axis tidal stream turbine, Renew. Energy 63 (2014) 222–235.
- [8] S. Tedds, Scale Model Testing of Tidal Stream Turbines: Wake Characterisation in Realistic Flow Conditions, University of Liverpool, 2014.
- [9] N. Kolekar, A. Vinod, A. Banerjee, On blockage effects for a tidal turbine in freesurface proximity, Energies 12 (17) (2019) 3325.
- [10] N. Kolekar, A. Banerjee, Performance characterization and placement of a marine hydrokinetic turbine in a tidal channel under boundary proximity and blockage effects, Appl. Energy 148 (2015) 121–133.
- [11] A.H. Birjandi, E.L. Bibeau, V. Chatoorgoon, A. Kumar, Power measurement of hydrokinetic turbines with free-surface and blockage effect, Ocean. Eng. 69 (2013) 9–17.
- [12] T. Stallard, R. Collings, T. Feng, J. Whelan, Interactions between tidal turbine wakes- experimental study of a group of three-bladed rotors, Phil. Trans. Roy. Soc. Lond.: Math. Phys. Eng. Sci. 371 (1985) (2013) 20120159.
- [13] P. Mycek, B. Gaurier, G. Germain, G. Pinon, E. Rivoalen, Experimental study of the turbulence intensity effects on marine current turbines behaviour. Part II: two interacting turbines, Renew. Energy 68 (2014) 876–892.
- [14] C. Gotelli, M. Musa, M. Guala, C. Escauriaza, Experimental and numerical investigation of wake interactions of marine hydrokinetic turbines, Energies 12 (16) (2019) 3188.
- [15] C.H. Frost, P.S. Evans, M.J. Harrold, A. Mason-Jones, T. O'Doherty,

- D.M. O'Doherty, The impact of axial flow misalignment on a tidal turbine, Renew. Energy 113 (2017) 1333–1344.
- [16] P.W. Galloway, L.E. Myers, A.S. Bahaj, Quantifying wave and yaw effects on a scale tidal stream turbine, Renew. Energy 63 (2014) 297–307.
- [17] B. Dou, M. Guala, L. Lei, P. Zeng, Wake model for horizontal-axis wind and hydrokinetic turbines in yawed conditions, Appl. Energy 242 (2019) 1383—1395.
- [18] P.K. Modali, N. Kolekar, A. Banerjee, Performance and wake characteristics of a tidal turbine under yaw, Int. J. Mar. Energy 1 (1) (2018).
- [19] S. Tatum, C. Frost, M. Allmark, D. O'doherty, A. Mason-Jones, P. Prickett, R. Grosvenor, C. Byrne, T. O'Doherty, Wave—current interaction effects on tidal stream turbine performance and loading characteristics, Int. J. Mar. Energy 14 (2016) 161–179.
- [20] V. Neary, B. Gunawan, D. Sale, Turbulent inflow characteristics for hydrokinetic energy conversion in rivers, Renew. Sustain. Energy Rev. 26 (2013) 437–445.
- [21] V.S. Neary, A.J. Odgaard, Three-dimensional flow structure at open-channel diversions, J. Hydraul, Eng. 119 (11) (1993) 1223–1230.
- [22] M. Lewis, S. Neill, P. Robins, M. Hashemi, S. Ward, Characteristics of the velocity profile at tidal-stream energy sites, Renew. Energy 114 (2017) 258–272.
- [23] M. Lewis, J. McNaughton, C. Márquez-Dominguez, G. Todeschini, M. Togneri, I. Masters, M. Allmark, T. Stallard, S. Neill, A. Goward-Brown, Power variability of tidal-stream energy and implications for electricity supply, Energy 183 (2019) 1061–1074.
- [24] F. O'Rourke, F. Boyle, A. Reynolds, D.M. Kennedy, Hydrodynamic performance prediction of a tidal current turbine operating in non-uniform inflow conditions, Energy 93 (2015) 2483–2496.
- [25] U. Ahmed, D. Apsley, I. Afgan, T. Stallard, P. Stansby, Fluctuating loads on a tidal turbine due to velocity shear and turbulence: comparison of CFD with field data, Renew. Energy 112 (2017) 235–246.
- [26] F. Porté-Agel, Y.-T. Wu, H. Lu, R.J. Conzemius, Large-eddy simulation of atmospheric boundary layer flow through wind turbines and wind farms, J. Wind Eng. Ind. Aerod. 99 (4) (2011) 154–168.
- [27] S. Wharton, J.K. Lundquist, Atmospheric stability affects wind turbine power collection, Environ. Res. Lett. 7 (1) (2012), 014005.
- [28] R. Wagner, I. Antoniou, S.M. Pedersen, M.S. Courtney, H.E. Jørgensen, The influence of the wind speed profile on wind turbine performance measurements, Wind Energy: Int. J. Progr. Appl. Wind Power Conver. Technol. 12 (4) (2009) 348–362.
- [29] R. Wagner, M. Courtney, J. Gottschall, P. Lindelöw-Marsden, Accounting for the speed shear in wind turbine power performance measurement, Wind Energy 14 (8) (2011) 993–1004.
- [30] G. Kavari, M. Tahani, M. Mirhosseini, Wind shear effect on aerodynamic performance and energy production of horizontal axis wind turbines with developing blade element momentum theory, J. Clean. Prod. 219 (2019)

- 368-376.
- [31] N. Sezer-Uzol, O. Uzol, Effect of steady and transient wind shear on the wake structure and performance of a horizontal axis wind turbine rotor, Wind Energy 16 (1) (2013) 1–17.
- [32] H. Makita, Realization of a large-scale turbulence field in a small wind tunnel, Fluid Dynam. Res. 8 (1991) 53–64.
- [33] W.-H. Lam, L. Chen, R. Hashim, Analytical wake model of tidal current turbine, Energy 79 (2015) 512–521.
- [34] J.V. Larssen, W.J. Devenport, On the generation of large-scale homogeneous turbulence, Exp. Fluid 50 (5) (2011) 1207–1223.
- [35] R.E.G. Poorte, A. Biesheuvel, Experiments on the motion of gas bubbles in turbulence generated by an active grid, J. Fluid Mech. 461 (2002) 127–154.
- [36] D.G. Goring, V.I. Nikora, Despiking acoustic Doppler velocimeter data, J. Hydraul. Eng. 128 (1) (2002) 117–126.
- [37] S.B. Pope, Turbulent Flows, Cambridge university press, 2000.
- [38] A. Vinod, A. Lawrence, A. Banerjee, Effects of free stream turbulence on tidal turbines. Part II turbine performance and near wake characteristics. 12th European Wave and Tidal Energy Conference, Cork, Ireland, 2017.
- [39] A. Bahaj, A. Molland, J. Chaplin, W. Batten, Power and thrust measurements of marine current turbines under various hydrodynamic flow conditions in a cavitation tunnel and a towing tank, Renew. Energy 32 (3) (2007) 407–426.
- [40] J.A. Colby, D. Corren, Detailed inflow measurements for kinetic hydropower systems in a tidal strait, in: Hydrovision, 2010.
- [41] N.D. Katopodes, Free-surface Flow: Environmental Fluid Mechanics, Butterworth-Heinemann. 2018.
- [42] C. Morris, D. O'Doherty, A. Mason-Jones, T. O'Doherty, Evaluation of the swirl characteristics of a tidal stream turbine wake, Int. J. Mar. Energy 14 (2016) 198–214.
- [43] A. Gupta, D. Lilley, N. Syred, Swirl Flows, Energy and Engineering Science Series, Abacus, London, 1984.
- [44] N Kolekar, SS Mukherji, A Banerjee, Numerical Modeling and Optimization of Hydrokinetic Turbine, in: Proceedings of the ASME 5th International Conference on Energy Sustainability, American Society of Mechanical Engineers, 2011, pp. 1211–1218. PartsAB, and C.DCUSA. WashingtonAugust, 7–10.
- [45] Suchi Subhra Mukherji, Nitin Kolekar, Arindam Banerjee, Rajiv Mishra, Numerical investigation and evaluation of optimum hydrodynamic performance of a horizontal axis hydrokinetic turbine, J. Renew. Sustain. Energy 3 (2011), https://doi.org/10.1063/1.3662100.
- [46] Zhen Hu, Xiaoping Du, Nitin Kolekar, Arindam Banerjee, Robust design with imprecise random variables and its application in hydrokinetic turbine optimization, Optim. Eng. 46 (3) (2014) 393–419, https://doi.org/10.1080/ 0305215X.2013.772603.
- [47] Matt Edmunds, Alison J. Williams, Ian Masters, Arindam Banerjee, James H. VanZwieten, A spatially nonlinear generalised actuator disk model for the simulation of horizontal axis wind and tidal turbines, Energy 194 (2020), https://doi.org/10.1016/j.energy.2019.116803.